Effects of (La, Sr) co-doping on electrical conduction and magnetic properties of $BiFeO_3$ nanoparticles*

Li Liu(刘莉)[1], Shouyu Wang(王守宇)[1,†], Zi Yin(殷子)[1], Weifang Liu(刘卫芳)[2], Xunling Xu(徐训岭)[2], Chuang Zhang(张闯)[1], Xiu Li(李秀)[1], and Jiabin Yang(杨佳斌)[1]

[1] *College of Physics and Materials Science, Tianjin Normal University, Tianjin* 300387, *China*

[2] *Department of Applied Physics, Institute of Advanced Materials Physics, Tianjin Key Laboratory of Low Dimensional Materials Physics and Preparing Technology, Faculty of Science, Tianjin University, Tianjin* 300072, *China*

(Received 14 January 2016; revised manuscript received 25 May 2016; published online 19 July 2016)

Multiferroic material as a photovoltaic material has gained considerable attention in recent years. Nanoparticles (NPs) $La_{0.1}Bi_{0.9-x}Sr_xFeO_y$ (LBSF, $x = 0$, 0.2, 0.4) with dopant Sr^{2+} ions were synthesized by the sol–gel method. A systematic change in the crystal structure from rhombohedral to tetragonal upon increasing Sr doping was observed. There is an obvious change in the particle size from 180 nm to 50 nm with increasing Sr substitution into LBFO. It was found that Sr doping effectively narrows the band gap from ~ 2.08 eV to ~ 1.94 eV, while it leads to an apparent enhancement in the electrical conductivity of LBSF NPs, making a transition from insulator to semiconductor. This suggests an effective way to modulate the conductivity of $BiFeO_3$-based multiferroic materials with pure phase by co-doping with La and Sr at the A sites of $BiFeO_3$.

Keywords: $BiFeO_3$, doping, conductivity, magnetic properties

PACS: 78.67.Bf, 77.84.–s, 75.75.–c **DOI:** 10.1088/1674-1056/25/9/097801

1. Introduction

Multiferroic materials which exhibit a coupling between magnetic and ferroelectric order parameters have been widely noted as materials promising for applications in multiple state memory elements, electric field controlled ferromagnetic resonance devices and transducers with magnetically modulated piezoelectricity.[1–4] Among all multiferroic materials studied so far, $BiFeO_3$ (BFO), having the perovskite-type structure with space group $R3C$,[5] possesses a superior ferroelectric polarization ($P_r \sim 100$ μC/cm^2), a high Curie temperature ($T_C \sim 1103$ K), and a high Neel temperature ($T_N \sim 643$ K). In addition, BFO is the one with simultaneous A site ferroelectric and B site G-type antiferromagnetic nature, and has attracted more and more attention recently. Primarily, BFO-based materials are of interest as multiferroics that are used for the development of magnetoelectric and photovoltaic materials, including thin-film materials and nanostructure sand compounds with BFO nanosized blocks.[6–8] For example, BFO nanoparticles (NPs) were used for BFO-graphene nanohybrids, which may find application due to their photocatalytic properties.[9]

Recently, several studies on A-site substitution of isovalent (La^{3+}, Nd^{3+}, and Sm^{3+}) or acceptor (Ca^{2+}, Ba^{2+}, and Pb^{2+}) cations for Bi and B-site substitution of donors (V^{5+}, Nb^{5+}, Mn^{4+}, or Ti^{4+}) for Fe have been carried out in order to improve the magnetic and ferroelectric properties.[10–13] As reported earlier, it is known[14] that in Ca-doped BFO, oxygen vacancies are produced that act as donor impurities to compensate the calcium acceptors. In order to maintain the electrical neutrality of the system, the oxygen vacancies can modify the electronic structure and the electrical conductivity. Similarly, several researchers have reported that doping Sr^{2+} can also change the properties of BFO because it can affect the structural, optical, dielectric, and magnetic properties.[15,16]

Converting sunlight into electricity is one of the most promising approaches to generate renewable energy. It has also been observed that doping can improve the photovoltaic properties of BFO by tuning the multiferroic properties and the leakage current.[17] In order to make use of BFO, it is necessary to modulate the electrical conductivity of BFO, i.e., converting it from an insulator to a semiconductor even to a conductor. Such kind of transition may make BFO a more comprehensive multiferroic material with a wide adjustable range of conductivity. Meanwhile, $SrFeO_3$ retains a metallic conductivity of $\sim 10^{-3}$ Ω/cm down to 4 K as reported by MacChesney *et al.*[18] So it is expected that Sr doping in BFO will increase the conductivity of the sample. There are only a few reported works on the substitution of divalent Sr ion at the trivalent Bi site of BFO NPs.[19,20] The reports demonstrated that the saturated magnetization of 20% Sr-doped BFO is 0.731 emu/g, which is higher than that of bulk BFO (0.229 emu/g), confirming that the substitution of Sr is an efficient way to enhance the magnetic properties of BFO.[21] In addition, the previously published works have focused on the substitution of low concentrations (below 20%)

*Project supported by the National Natural Science Foundation of China (Grant Nos. 11104202 and 51572193).

†Corresponding author. E-mail: shouyu.wang@yahoo.com

© 2016 Chinese Physical Society and IOP Publishing Ltd

of Sr in BFO, and higher concentration Sr doping in NPs (up to 20%) has rarely been reported. Especially, there is no report on the effects of Sr doping on the leakage current for BFO NPs. In the present study, we focus on $La_{0.1}Bi_{0.9-x}Sr_xFeO_y$ (LBSF) NPs with Sr ions up to 40% and the effect of varying Sr concentration on the optical, leakage current, and magnetic properties.

In this work, we have synthesized high quality $La_{0.1}Bi_{0.9-x}Sr_xFeO_y$ ($x = 0$, 0.2, 0.4, as abbreviated to LBFO, LBSF-20, and LBSF-40, respectively) NPs via a facile sol–gel method. The optical, leakage, and magnetic properties of the NPs have been investigated. In the Sr-doped LBFO, the leakage current density of NPs is significantly increased and the largest leakage current density ($\sim$ 16 mA/cm^2) is observed in the LBSF-40 NPs. Thus the electrical conductivity of the LBSF NPs shows a clear signature of transition from an insulating state to a semiconducting state. The magnetic properties have been greatly improved and the saturated magnetization (M_S) for LBSF-40 is 8.77 emu/g.

2. Experiments

LBSF NPs were synthesized by the sol–gel method. High purity grade $Bi(NO_3)_3{\cdot}5H_2O$, $Fe(NO_3)_3{\cdot}9H_2O$, $La(NO_3)_3{\cdot}6H_2O$, and $Sr(NO_3)_2$ in an appropriate molar ratio were mixed in analytical grade ethylene glycol to prepare the precursor solution. Analytical grade tartaric acid was added to the solution in 1:1 molar ratio with respect to the precursors, and the mixture was stirred continuously at 70 °C for 3 h. The solution was a transparent, reddish-brown, and clear sol. Then it was placed in a drying oven at 90 °C for 4 h until the clear sol completely turned to a yellowish-brown gel. The gel was further dried at 140 °C for 3 h, then annealed at 400 °C for 2 h, and finally ground into powder. Subsequently the powder was calcined at 600 °C in air for 2 h to obtain NPs.

The crystalline structure analysis of the NPs was carried out by x-ray diffraction (XRD, Rigaku D/MAX-2500 diffractometer with Cu $K\alpha$ radiation). The average particle size and microstructural properties of the NPs were investigated by a transmission electron microscope (TEM) (JEM-2100F). High resolution TEM (HRTEM) and the corresponding selected area electron diffraction (SAED) patterns were recorded by the same instrument. Magnetic characterization of the samples was done with a magnetic property measurement system (MPMS) (SQUID-VSM made by Quantum Design). The UV–vis absorption spectrum of our NPs was obtained by a Shimadzu UV-3600UV-VIS-NIR spectrophotometer. To study the electrical properties, the samples were pressed into pellets by compaction of powders in a uniaxial press, and the pellets were sintered for half an hour at 600 °C. The dielectric properties were measured by a precise impendence analyzer WK 6400 with an ac signal of 1000 mV. The leakage current curve was evaluated using an Axiacct model TF 2000 ferroelectric analyser. All the measurements were carried out at room temperature.

3. Results and discussion

The observed, calculated, and difference XRD patterns for LBFO, LBSF-20, and LBSF-40 obtained from the Rietveld refinement are shown in Fig. 1(a). All the samples have good crystallization with no impurity phase. The LBFO sample crystallizes in the rhombohedral structure with space group $R3C$. Figures 1(b) and 1(c) show the enlarged views of the diffraction peaks located at about $2\theta \approx 32°$ and $2\theta \approx 39°$, respectively. We can see that with Sr doping in LBFO, doubly split peaks near 32° and 39° merge gradually and a small shift to a higher angle is observed in the vicinity of 32°, indicating a structural distortion due to La and Sr co-doping in BFO NPs, as Sr (1.12 Å) has a larger ionic radius than Bi (1.03 Å). A similar type of phase transition has also been reported for Nd, Eu, Pb, and Ba-doped BFO ceramics.[11,22–24] The crystal structure parameters derived from refinement are listed in Table 1. These parameters clearly indicate a structural phase transition from a distorted rhombohedral to a tetragonal structure with the increase of the Sr content in LBFO.

To investigate the morphology of the as-obtained NPs, we carried out transmission electron microscopy analysis. Figures 2(a) and 2(b) show the TEM micrographs, HRTEM images, and SAED patterns of LBFO and LBSF-20 NPs, respectively. The LBFO exhibits a nearly spherical morphology, while some agglomerations in nature are found for the LBSF-20. The average particle size determined from the TEM micrographs is nearly 180 nm for LBFO, 100 nm for LBSF-20, and 50 nm for LBSF-40. It demonstrates that the crystal size sharply decreases with the increase of the Sr doping concentration. As we all know, the grain growth depends upon the compression of the oxygen vacancies and the diffusion rate of the ions.[25] With increasing dopant concentration, the crystal growth of the NPs might be suppressed because Sr has a larger ionic radius, which results in the formation of smaller particles. So the average grain size of the LBSF NPs is extraordinarily smaller compared to that of the LBFO. The upper and lower insets in Figs. 2(a) and 2(b) show the HRTEM images and the SAED patterns of LBFO and LBSF-20 NPs, respectively. Clear lattice fringes are visible, suggesting a high degree of crystallinity in our NPs. The distances between two lattice planes are found to be around 0.399 nm and 0.288 nm, which correspond to the (101) and (012) lattice planes of LBFO and LBSF-20, respectively. The lower insets indicate the single-crystalline nature of LBFO and the polycrystalline nature of LBSF-20.

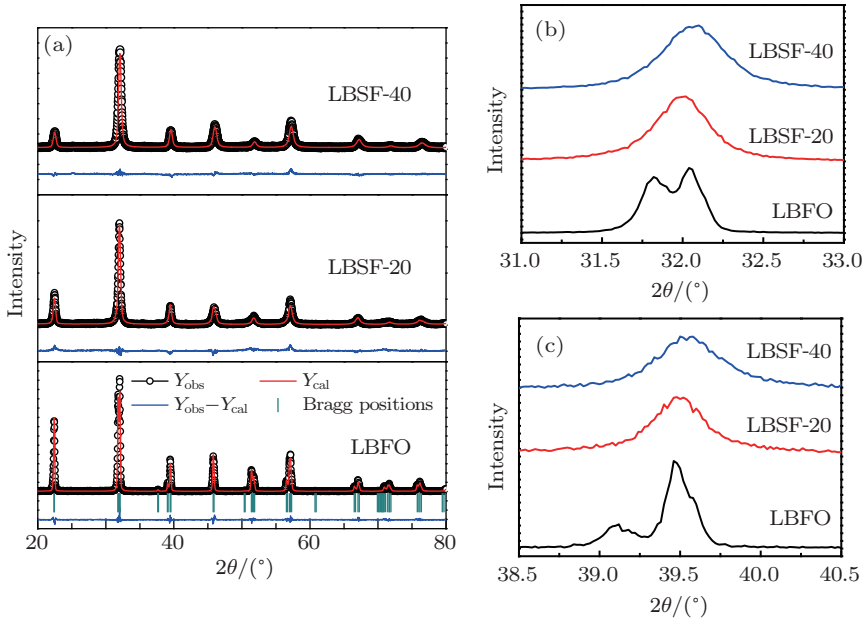


Fig. 1. (color online) (a) The observed, calculated, and difference Rietveld refined XRD patterns of $La_{0.1}Bi_{0.9-x}Sr_xFeO_y$ ($x = 0$, 0.2, 0.4) nanoparticles. Enlarged views of the diffraction peaks located at about (b) $2\theta \approx 32°$ and (c) $2\theta \approx 39°$.

Table 1. Structure parameters obtained from Rietveld refinement of samples.

Compound	Structure	a/Å	b/Å	c/Å	α/(°)	β/(°)	γ/(°)	Fe–O–Fe
LBFO	$R3C$	5.5723(4)	5.5723(4)	13.7969(7)	90	90	120	155.15°
LBSF-20	$P4/mmm$	3.9488(8)	3.9488(8)	3.9238(3)	90	90	90	180°
LBSF-40	$P4/mmm$	3.9412(8)	3.9412(8)	3.9234(4)	90	90	90	180°

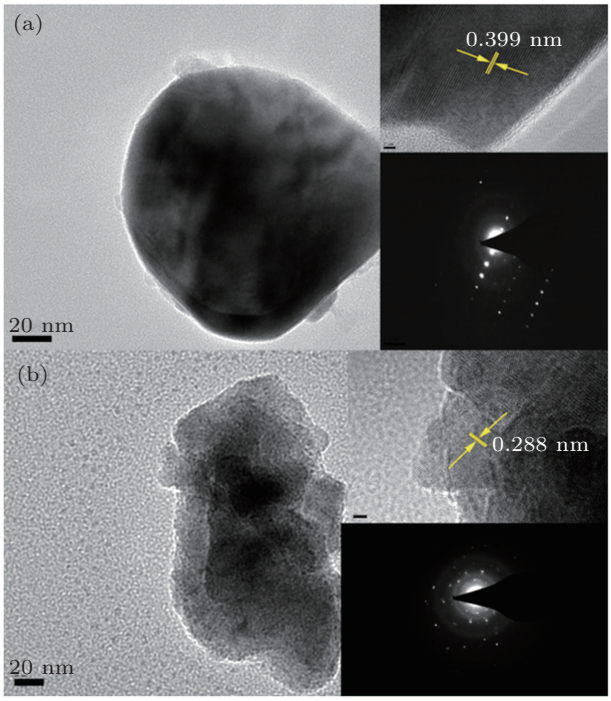


Fig. 2. (color online) TEM photographs of the nanoparticles $La_{0.1}Bi_{0.9-x}Sr_xFeO_y$: (a) $x = 0$, (b) $x = 0.2$. The upper and lower insets show the HRTEM image and the SAED pattern of LBFO and LBSF-20 nanoparticles, respectively.

It is important to investigate the electronic structure of Sr^{2+} doped into LBFO because the heterovalent substitution-induced defects may cause high leakage current and narrow band gap. Figure 3 shows the UV–vis absorption spectra of the LBSF NPs measured at room temperature. To investigate more precisely the details of the band structures of these NPs, the band gaps (E_g) of the NPs are calculated according to the following equation:[26]

$$\alpha h\nu = C(h\nu - E_g)^n, \tag{1}$$

where C is a constant, $h\nu$ is the photon energy, and α is the absorption coefficient. The value of n depends on the nature of the electronic transition responsible for absorption. Because BFO is a direct band gap semiconductor material, n takes the value of 1/2. The plots of $(\alpha h\nu)^2$ against $h\nu$ are shown in the inset of Fig. 3. The absorption edge of the crystal is shifted towards the larger wavelength (low energy) with respect to that of the LBFO NPs, indicating that the dopant ions cause a significant change in the band structure. In the calculation, the energy band gap shows a linear change from 2.08 eV for LBFO to 1.94 eV for LBSF-40, which makes Sr-doped LBFO a potential photovoltaic material. These band gaps are relatively lower as compared to their counterparts, being 2.20 eV for undoped BFO,[27] 2.13 eV for Ca-doped BFO,[28] and 2.16 eV for Pd-doped BFO.[29] It is well known that the properties of optical absorption (UV–vis) of semiconductors are relevant to their electronic structure features and hence are the key factors in determining their band gaps. The Fe–O–Fe bond angle is an important factor affecting the change of the band gap. It

has been reported that a larger Fe–O–Fe bond angle (towards 180°) would increase the bandwidth of the occupied and unoccupied bands, and therefore reduce the band gap of BFO.[30] Doping Sr in LBFO can have a vast stimulating effect on the electronic structure. Because of the structural phase transition from distorted rhombohedral to tetragonal phase, the Fe–O–Fe bond angle is expanded from 155.15° to 180°. With the increasing content of Sr^{2+} ions, the band gap of the NPs is steadily reduced. The decrease in the band gap can be ascribed to the rearrangement of the molecular orbitals induced by dopant Sr^{2+} ions. Another important reason is that the Sr substitution may lead to formation of defects and oxygen vacancies for the requirement of charge compensation. Doping acceptor ions Sr^{2+} in LBFO would generate oxygen vacancies to neutralize the charge produced due to the mechanism of charge compensation. The main process can be described as follows:

$$2\mathrm{SrO} \rightarrow 2(\mathrm{Sr_{Bi}})' + 2\mathrm{O_O^{\times}} + \mathrm{V_O^{\bullet\bullet}}. \quad (2)$$

It reveals that the higher substitution of Bi^{3+} by Sr^{2+} produces more oxygen vacancies. It is reported that the energy levels corresponding to these oxygen vacancies are lower than the adjacent Fe 3d levels, resulting in the sub-bandgap defect states.[31] To better understand the variation of the band gap with the Sr concentration in our La, Sr co-doped NPs, a schematic diagram of the qualitative structure of the electronic energy band is shown in the inset of Fig. 3. The observed shrinking of the band gap is possibly caused by the formation of an impurity band resulting from the high Sr doping concentration. So, with increasing the concentration of Sr^{2+} ions, the band gap is clearly reduced.

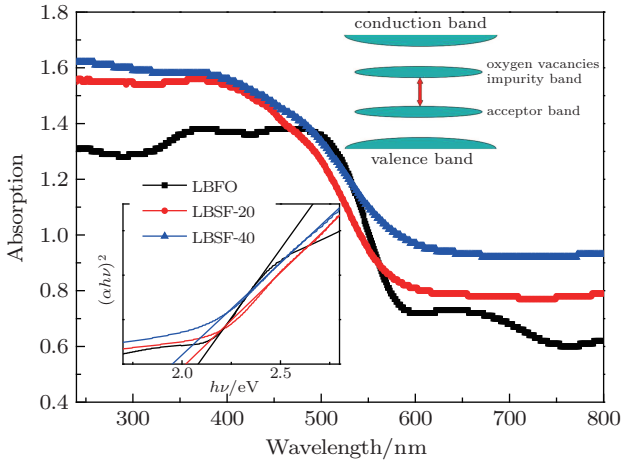


Fig. 3. (color online) UV–vis absorbance of $La_{0.1}Bi_{0.9-x}Sr_xFeO_y$ ($x = 0, 0.2, 0.4$) nanoparticles. The lower inset depicts the $(\alpha h\nu)^2$ versus $h\nu$ plot of all nanoparticles, where the intercept of the extrapolated absorption edge on the energy scale (x axis) gives the band gap of the nanoparticles. The upper inset is a schematic diagram of a possible mechanism for the electronic energy band.

Figure 4 plots the leakage current density (J) as a function of the applied electric field (E) at room temperature. It is demonstrated that the leakage current density becomes larger with increasing Sr doping concentration in LBFO in the range of the scanning electric field. The leakage current densities of LBFO, LBSF-20, and LBSF-40 under the voltage of 250 V are 0.3 μA/cm^2, 2.3×10^2 μA/cm^2, and 1.6×10^4 μA/cm^2, respectively. This clearly reveals that the leakage current density can be effectively increased with Sr-doping in LBFO, and the value of LBSF-40 is approximately five orders of magnitude larger than that of LBFO. Therefore the conductivity of BFO could be well modulated by La and Sr co-doping to realize a transition from an insulator to a semiconductor. The mechanism of our modulation in La, Sr co-doping BFO NPs is mainly based on electronic conduction as a consequence of the naturally produced oxygen vacancies. An electronic conductor–insulator transition was also observed in Ca-doped BFO thin films by Kaveh *et al.*[32] The conduction mechanisms of the present samples are further investigated by plotting $\log J$ versus $\log E$ in the inset of Fig. 4. It can be seen that the Ohmic conduction mechanism dominates the electrical transportation in our samples in the range of 0–250 V.

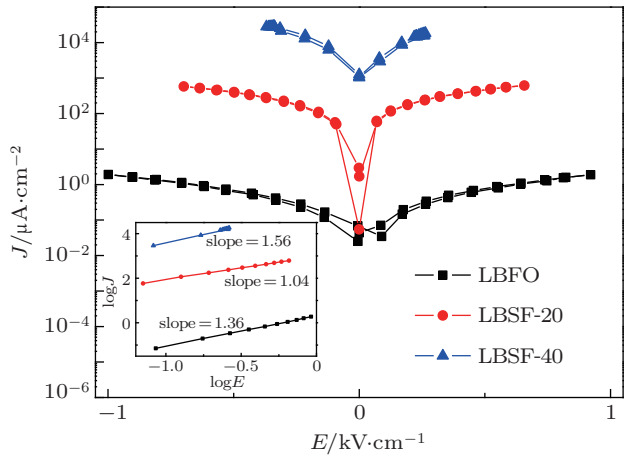


Fig. 4. (color online) Leakage current as a function of applied electric field (J–E) and the log(J) versus log(E) plot (in the inset) for $La_{0.1}Bi_{0.9-x}Sr_xFeO_y$ ($x = 0$, 0.2, 0.4) nanoparticles at room temperature.

To completely understand the enhancement of the current density in La and Sr co-doped BFO NPs, one possible factor that controls the transport properties should be considered. It is well known that in the perovskite structure materials, the ionization process of the oxygen vacancy (V_O) will create conducting electrons (e'), thus contributing to the leakage current. The process can be described as follows:

$$V_O \rightarrow V_O^{\bullet} + e', \quad (3)$$

$$V_O^{\bullet} \rightarrow V_O^{\bullet\bullet} + e'. \quad (4)$$

Furthermore, the oxygen vacancies as discussed above are easily created in order to satisfy the charge balance upon the doping of Sr. The main process can be described by Eq. (2). The formation of oxygen vacancies provides free charge carriers,

meanwhile the migration of the charge carriers under an appropriate electric field would become stronger. Moreover, the activated electrons by the external potential would be trapped by the oxygen vacancies and contribute to the leakage current.[33] Therefore, according to the above analysis, increased Sr doping leads to the increase of the leakage current.

The ferroelectric hysteresis loops of the Sr-doped LBFO NPs at room temperature are shown in Fig. 5. As a result of the higher electrical conductivity in the Sr-doped LBFO NPs, the applied electric field is gradually decreased in ferroelectric hysteresis loop measurements, as shown in Fig. 5. Under the applied field of 35 kV/cm, the remnant polarization ($2P_r$) of the LBFO is found to be 1.23 μC/cm^2. The *P*–*E* loops of the LBSF-20 and LBSF-40 NPs are still round in shape, which originates from the higher electrical conductivity in the LBSF-20 and LBSF-40 NPs. The ferroelectric properties of the LBFO NPs, which show typical and saturated ferroelectric loop characteristics to some extent, are correlated to the low leakage current density.[34] In addition, as discussed above in Fig. 4, increased Sr doping leads to the increase of the leakage current, as a consequence, it will increase the electrical conductivity of the samples. Therefore, the electrical conductivity of BFO could be well modulated by La and Sr co-doping to realize a transition from an insulator to a semiconductor in the BFO system.

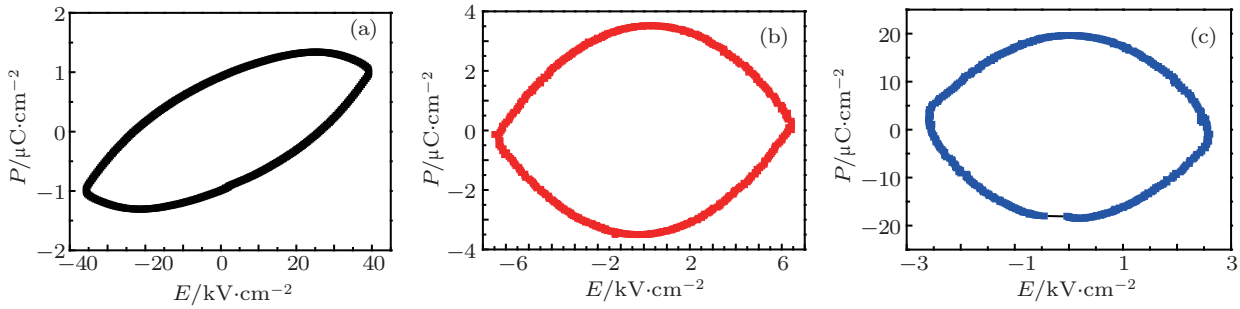


Fig. 5. (color online) Room temperature ferroelectric hysteresis loops for (a) LBFO, (b) LBSF-20, and (c) LBSF-40.

The dielectric properties of the Sr-doped LBFO NPs measured at room temperature in the frequency range from 1 kHz to 1 MHz are shown in Fig. 6. It is seen that the dielectric constants of LBFO, LBSF-20, and LBSF-40 are 277, 486, and 1025 at 1 kHz, respectively. The dielectric losses of LBFO, LBSF-20, and LBSF-40 are 0.13, 2.56, and 380.81 at 1 kHz, respectively. The dielectric constants of all compositions are observed to decrease sharply with the increase of the frequency in the low frequency region and then tend to a certain value in the high frequency region. This phenomenon can be explained by the space charge relaxation effect.[35] The space charge is able to follow the applied field in the low frequency region (1 kHz–10 kHz), while it does not have enough time to undergo relaxation in the high frequency region (10 kHz–1 MHz). A large dielectric constant and dielectric loss for the LBSF NPs are correlated with the large leakage current density of these NPs. The dielectric constant and the dielectric loss become large with increasing Sr doping concentration at low frequency, which can be understood on the following basis: replacement of Bi^{3+} ions by Sr^{2+} ions in LBFO requires charge compensation, which can be realized by creating anion vacancies (i.e., oxygen vacancies). In addition, at low frequencies, the dipoles are able to follow the applied field. Therefore, doping of Sr^{2+} is expected to introduce more oxygen vacancies, increasing the probability of the hoping conduction mechanism and resulting in a high dielectric constant. A similar trend has been reported in Mn and Sr co-doped BFO by Yu *et al.*[36]

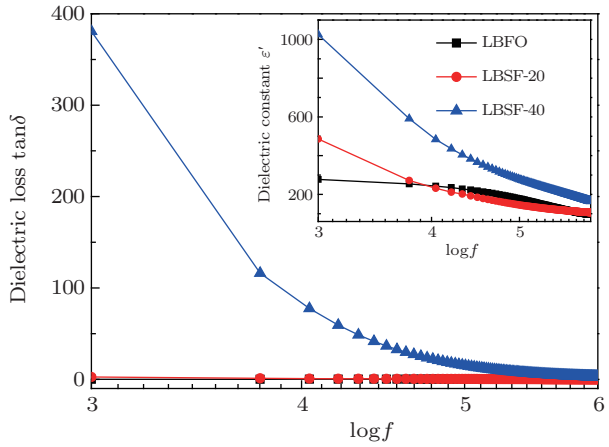


Fig. 6. (color online) Frequency response of dielectric loss (tanδ) for all nanoparticles $La_{0.1}Bi_{0.9-x}Sr_xFeO_y$ ($x = 0$, 0.2, 0.4), the inset depicts the dielectric constant (ε') versus frequency ranging from 1 kHz to 1 MHz at room temperature.

Figure 7 shows the *M*–*H* curves of the LBSF NPs at room temperature and the inset shows the saturation magnetization (M_S) of all samples. It is obvious that the M_S of the NPs is distinctly influenced by Sr doping. The M_S of LBFO, LBSF-20, and LBSF-40 are 0.60 emu/g, 2.28 emu/g, and 8.77 emu/g, respectively. Obviously, the M_S has been greatly improved upon Sr doping. Based on the magnetic structure of BFO, the improvement of magnetization in our LBSF NPs is deduced as follow. Firstly, the particle size would also give rise to modula-

tion in M_S. It is suggested that in a nanoparticle system, the reduced particle size can modulate the periodic spiral-modulated spin structure, then it will induce a larger M_S.[37] As discussed above in Fig. 2, the particle size gradually decreases with increasing dopant concentration, as a consequence, it will enhance the M_S in our NPs. This phenomenon was also reported by Wang *et al.*,[21] the M_S of pure BFO and 20% Sr-doped BFO were 0.21 emu/g and 0.73 emu/g at an applied magnetic field of 10 kOe, respectively. At the same time, in the nanoparticle structure, the ratio of surface to volume becomes very large because of the decreasing particle size with Sr doping, which increases the tangible contribution of the uncompensated surface spins[38] to the particle's overall magnetization and thus enhances the magnetization of our samples. Therefore, increasing the Sr concentration results in an enhancement of the magnetic properties. Compared with other co-doped BFOs, such as Nd and La co-doped BFO[22] and Nb and Sr co-doped BFO,[39] the La and Sr co-doped BFO has a higher saturated magnetization.

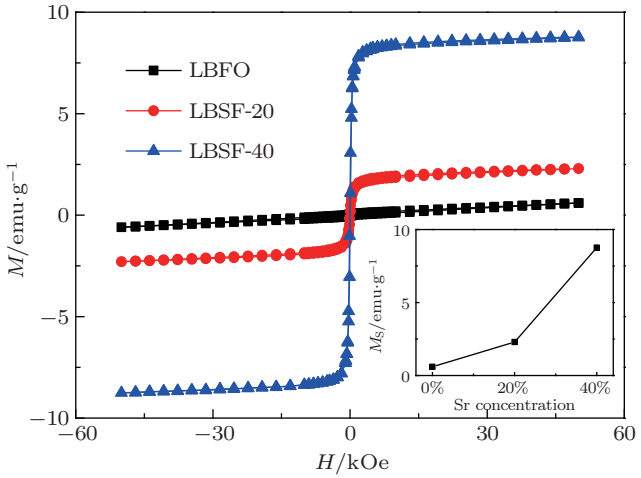


Fig. 7. (color online) The field dependent magnetization hysteresis (M–H) loops of $La_{0.1}Bi_{0.9-x}Sr_xFeO_y$ ($x = 0$, 0.2, 0.4) nanoparticles at room temperature, and the inset shows the saturation magnetization (M_S) of all nanoparticles.

4. Conclusion

Single-phase LBFO perovskite NPs and Sr-doped LBFO NPs have been successfully prepared by the sol–gel method. The average particle size decreases obviously with Sr doping. The M–H measurements reveal that the saturation magnetization of the NPs is distinctly influenced by the increase of the Sr doping concentration. Both dielectric constant and dielectric loss factors of all compositions decrease gradually with the increase of the frequency. Significant improvements, such as increased leakage current density and reduced band gap, are observed for the LBSF NPs. Such vast modulation of the conductivity may further enhance the application of the BFO structure from random access memories to solar cells and even electronic and photonic devices in a drastic fashion.

References

[1] Cheong S W and Mostovoy M 2007 *Nat. Mater.* **6** 13
[2] Fiebig M and Haston K 2002 *Nature* **419** 818
[3] Coey J M D, Douvalis A P, Fitzgerald C B and Venkatesan M 2004 *Appl. Phys. Lett.* **84** 1332
[4] Kimura T, Sekio Y and Nakamura H 2008 *Nat. Mater.* **7** 291
[5] Hill N A 2000 *J. Phys. Chem. B.* **104** 6694
[6] Wang J, Neaton J B, Zheng H, Nagarajan V, Ogale S B, Liu B, Viehland D, Vaithyanathan V, Schlom D G, Waghmare U V, Spaldin N A, Rabe K M, Wuttig M and Ramesh R 2003 *Science* **299** 1719
[7] Li S, Nechache R, Harnagea C, Nikolova L and Rose F 2012 *Appl. Phys. Lett.* **101** 192903
[8] Basu S R, Martin L W, Chu Y H, Gajek M, Ramesh R, Rai R C, Xu X and Musfeldt J L 2008 *Appl. Phys. Lett.* **92** 091905
[9] Li T, Shen J, Li N and Ye M 2013 *Mater. Lett.* **91** 42
[10] Lan C, Jiang Y and Yang S 2011 *J. Mater. Sci.* **46** 734
[11] Yuan G L and Wing S 2006 *J. Appl. Phys.* **100** 024109
[12] Yan Z, Wang K F, Qu J F and Wang Y 2007 *Appl. Phys. Lett.* **91** 082906
[13] Agarwal R A, Sanghi S and Ashima 2011 *J. Appl. Phys.* **110** 073909
[14] Gavriliuk A G, Struzhkin V V, Lyubutin I S, Ovchinnikov S G, Hu M Y and Chow P 2008 *Phys. Rev. B* **77** 155112
[15] Kundys B, Maignan A, Martin C, Nguyen N and Simon C 2008 *Appl. Phys. Lett.* **92** 112905
[16] Singh P, Park Y A, Sunga K D, Hura N, Jung J H, Nohb W S, Kimb J Y, Yoonc J and Jo Y 2010 *Solid State Commun.* **150** 431
[17] Yang S Y, Seidel J, Byrnes S J, Shafer P, Yang C H, Rossell M D, Yu P, Chu Y H, Scott J F, Ager J W, Martin L W and Ramesh R 2010 *Nat. Nanotechnol.* **5** 143
[18] MacChesney J B, Sherwood R C and Potter J F 1965 *J. Chem. Phys.* **43** 1907
[19] Bhushan B, Basumallick A, Vasanthacharya N Y, Kumar S and Das D 2010 *Solid State Sci.* **12** 1063
[20] Brinkman K, Iijima T and Takamura H 2010 *Solid State Ionics* **181** 53
[21] Wang B, Wang S, Gong L and Zhou Z 2012 *Ceram. Int.* **38** 6643
[22] Pandit P, Satapathy S, Gupta P K and Sathe V G 2009 *J. Appl. Phys.* **106** 114105
[23] Reddy V R, Kothari D, Gupta A and Gupta S M 2009 *Appl. Phys. Lett.* **94** 082505
[24] Makhdoom A R, Akhtar M J, Rafiq M A and Hassan M M 2012 *Ceram. Int.* **38** 3829
[25] Brinkman K, Iijima T, Nishida K, Katoda T and Funakubo H 2007 *Ferroelectrics* **357** 1
[26] Wang D H, Goh W C, Ning M and Ong C K 2006 *Appl. Phys. Lett.* **88** 212907
[27] Zhang H, Liu W F, Wu P, Hai X, Guo M, Wang S Y, Gao J, Xi X J, Wang X, Guo F, Xu X L, Wang C, Liu G Y and Chu W G 2014 *J. Name.* **6** 18
[28] Wang X, Wang S Y, Liu W F, Xi X J, Zhang H, Guo F, Xu X L, Li M, Liu L, Zhang C, Li X and Yang J B 2015 *J. Nanopart. Res.* **17** 209
[29] Han Y L, Liu W F, Wu P, Xu X L, Guo M C, Rao G H and Wang S Y 2016 *J. Alloys. Compd.* **661** 115
[30] Borisevich A Y, Chang H J, Huijben M, Oxley M P, Okamoto S, Niranjan M K, Burton J D, Tsymbal E Y, Chu Y H, Yu P, Ramesh R, Kalinin S V and Pennycook S J 2010 *Phys. Rev. Lett.* **105** 087204
[31] Hauser A J, Zhang J, Mier L, Ricciardo R, Woodward P M, Gustafson T L, Brillson L J and Yang F Y 2008 *Appl. Phys. Lett.* **92** 222901
[32] Kawae T, Terauchi Y, Tsuda H, Kumeda M and Morimoto A 2009 *Appl. Phys. Lett.* **94** 112904
[33] Qi X, Dho J, Tomov R, Blamire M G and MacManus-Driscoll J L 2005 *Appl. Phys. Lett.* **86** 062903
[34] Wang Y P, Zhou L, Zhang M F, Chen X Y, Liu J M and Liu Z G 2004 *Appl. Phys. Lett.* **84** 1731
[35] Rodrigues H O, Pires Jr G F M, Almeida J S, Sancho E O, Ferreira A C, Silva M A S and Sombra A S B 2010 *J. Phys. Chem. Solids.* **71** 1329
[36] Yu X and An X 2009 *Solid State Commun.* **149** 711
[37] Guo M C, Liu W F, Xu X L, Wu P, Zhang H, Han Y L, Rao G H and Wang S Y 2015 *J. Nanopart. Res.* **17** 1
[38] Huang F Z, Wang Z J, Lu X M, Zhang J T, Min K L, Lin W W, Ti R X, Xu T T, He J, Yue C and Zhu J S 2013 *Sci. Rep.* **3** 2907
[39] Reetu, Agarwal A, Sanghi S, Ashima, Ahlawat N and Monica 2012 *J. Appl. Phys.* **111** 113917